RSC Advances

PAPER

View Article Online
View Journal | View Issue

Cite this: *RSC Adv.*, 2025, **15**, 39951

Unveiling ferroelectric and altermagnetic coexistence in multiferroic $HfMnO_3$ perovskite

Abid Zaman, *[a] Salhah Hamed Alrefaee,[b] Shirin Shomurotova,[c] Anvar Nurmuhammedov,[d] Salah Knani,*[e] Vineet Tirth,[fg] Ali Algahtani[fh] and Noureddine Elboughdiri[i]

Multiferroic materials, which simultaneously exhibit electric and magnetic ordering, have garnered increasing attention due to their potential to revolutionize next-generation spintronic, memory, and multifunctional devices. Their unique ability to couple electric polarization and magnetic states offers low-power operation, electric field control of magnetism, and enhanced device scalability. Among these, altermagnetic multiferroics are particularly promising for enabling spin-polarized transport without stray fields. In this context, we have systematically investigated the structural, electronic, ferroelectric, and optical properties of the trigonal *R*3*c*-phase $HfMnO_3$ using first-principles density functional theory. The compound is found to be thermodynamically and dynamically stable, with a Goldschmidt tolerance factor of 0.88 supporting a distorted perovskite framework. The spin-resolved band structure revealed energy-dependent spin splitting without net magnetization, which is characteristic of altermagnetic behavior. Furthermore, our Berry phase calculations predict a robust spontaneous polarization of approximately 104 μC cm^{-2} along the [111] direction, positioning $HfMnO_3$ as a strong ferroelectric candidate. Remarkably, the polarization-switched state retains both dynamic and electronic stability while preserving the altermagnetic signatures, confirming the multiferroic nature of the material. Optical analyses show high UV absorption, a notable refractive index, and plasmonic features above 7.5 eV, suggesting potential applications in optoelectronics and UV photodetectors. These findings establish $HfMnO_3$ as a promising altermagnetic multiferroic oxide for multifunctional applications in spintronic and optoelectronic technologies.

Received 2nd July 2025
Accepted 5th October 2025

DOI: 10.1039/d5ra04705f

rsc.li/rsc-advances

Introduction

The recent emergence of altermagnetism has introduced a novel and fundamentally distinct class of magnetic ordering in condensed matter systems. Unlike conventional ferromagnets, which exhibit net magnetization, or antiferromagnets, which feature spin-compensated but often spin-degenerate band structures, altermagnets are characterized by collinear magnetic moments arranged in a crystal-symmetry-induced compensated configuration that breaks both time-reversal symmetry and spin-rotation symmetry and yet preserves spatial inversion or certain combined symmetries. This results in spin–split electronic bands even in the absence of macroscopic magnetization, a phenomenon not observed in classical antiferromagnets.[1–3] The key feature of altermagnets is their non-relativistic spin polarization, which arises purely from crystal symmetry and magnetic ordering, rather than from spin–orbit coupling. This allows for the anisotropic spin transport, highly spin-polarized currents, and robust control of spin degrees of freedom without the drawbacks of stray magnetic fields.[4] Notable examples of altermagnetic materials include MnTe, RuO_2, CrSb, and TiAu, in which spin-polarized band structures have been predicted or experimentally confirmed.[5–8] Besides, many studies have indicated the importance of altermagnetism.[9–11] These systems are particularly promising for dissipationless spintronic devices, where spin information can be manipulated efficiently and robustly, even in the absence of external magnetic fields.

[a]*Department of Physics, Riphah International University Islamabad, 44000, Pakistan. E-mail: zaman.abid87@gmail.com*

[b]*Department of Chemistry, College of Science in Yanbu Governorate, Taibah University, Saudi Arabia*

[c]*Department of Chemistry Teaching Methods, Tashkent State Pedagogical University Named After Nizami, Bunyodkor Street 27, Tashkent, Uzbekistan*

[d]*Western Caspian University, Baku, Azerbaijan*

[e]*Center for Scientific Research and Entrepreneurship, Northern Border University, Arar 73213, Saudi Arabia. E-mail: saleh.kenani@nbu.edu.sa*

[f]*Mechanical Engineering Department, College of Engineering, King Khalid University, Abha 61421, Aseer, Kingdom of Saudi Arabia*

[g]*Centre for Engineering and Technology Innovations, King Khalid University, Abha 61421, Aseer, Kingdom of Saudi Arabia*

[h]*Research Center for Advanced Materials Science (RCAMS), King Khalid University, Guraiger, P.O. Box 9004, Abha-61413, Aseer, Kingdom of Saudi Arabia*

[i]*Chemical Engineering Department, College of Engineering, University of Ha'il, P.O. Box 2440, Ha'il 81441, Saudi Arabia*

Parallel to these developments, ferroelectric materials, characterized by a spontaneous electric polarization that can be reversed by an external electric field, have long been studied for their applications in non-volatile memory, piezoelectric sensors, and energy-harvesting technologies. In recent years, thin films of $BiFeO_3$ have exhibited remarkably high ferroelectric polarizations surpassing those found in classical ferroelectric materials such as $BaTiO_3$ and $PbTiO_3$.[12–14] These enhanced polarization values correlate well with the significant atomic displacements observed in the crystal structure. Interestingly, such behavior appears to differ from earlier findings on the bulk $BiFeO_3$, where much smaller polarization values were reported.[15] The discrepancy between thin film and bulk forms remains a subject of ongoing discussion. Notable magnetization values, reaching approximately 1 μB per formula unit, have been detected, particularly in films with reduced thickness,[8] and these magnetic features are accompanied by strong magnetoelectric coupling effects.

The combination of altermagnetism and ferroelectricity in a single material presents a compelling opportunity to explore a new class of multiferroic altermagnets. Such systems would unite the benefits of zero-*net*-magnetization spintronics with electric-field-tunable polarization, offering rich physics and potential device applications. While still relatively unexplored, a few theoretical efforts have proposed that certain materials, such as $BaCuF_4$ and $BiFeO_3$, may simultaneously support spin-polarized compensated magnetic states and ferroelectricity.[16,17] Further, some 2D and other materials have been explored, which have altermagnet behaviors along with ferroelectricity.[18–20] These studies have many limitations, and the materials either have small spontaneous polarization or small critical temperature.

Herein, we investigate a multiferroic $HfMnO_3$ perovskite exhibiting both altermagnetic and ferroelectric properties. To the best of our knowledge, there have been no prior reports regarding this. Using density functional theory (DFT), we have performed comprehensive calculations of its electronic band structure, revealing spin-polarized states indicative of altermagnetic ordering. In addition, we have evaluated its piezoelectric response and spontaneous electric polarization using the Berry phase method, confirming the presence of robust ferroelectricity. The coexistence of these ferroic orders in a single-phase perovskite offers promising prospects for magnetoelectric coupling, spin-charge conversion, and the design of next-generation multifunctional devices.

Computational techniques

First-principles calculations based on Density Functional Theory (DFT) were performed using the Vienna *Ab initio* Simulation Package (VASP) to investigate the structural, magnetic, ferroelectric, and optical properties of $HfMnO_3$. The projector augmented-wave (PAW) method was employed to treat the interactions between ions and electrons, and the generalized gradient approximation (GGA) with the Perdew–Burke–Ernzerhof (PBE) exchange–correlation functional was used throughout the study. To account for strong on-site Coulomb interactions in the localized Mn 3d states, the GGA + U approach was adopted using the Dudarev scheme, with an effective Hubbard parameter $U_{\text{eff}} = 4.0$ eV applied to the Mn atoms. The plane-wave energy cutoff was set to 500 eV, and a Monkhorst–Pack *k*-point mesh of $6 \times 6 \times 6$ was used for Brillouin zone sampling during structural optimization and electronic calculations. The atomic structure was fully relaxed until the forces on each atom were less than 0.001 eV $Å^{-1}$ and the total energy converged within 10^{-6} eV. Dynamic stability was assessed by computing the phonon dispersion using the finite displacement method, as implemented in the PHONOPY code, with a $2 \times 2 \times 2$ supercell. To investigate the ferroelectric behavior of $HfMnO_3$, we employed the Berry phase approach within the framework of the modern theory of polarization. In this method, the spontaneous polarization is evaluated as the difference between the total Berry phase polarization of the relaxed non-centrosymmetric ferroelectric structure and that of the centrosymmetric (paraelectric) reference structure. The centrosymmetric structure was generated by symmetrizing the atomic positions to restore inversion symmetry, while the ferroelectric configuration was obtained from full structural relaxation without symmetry constraints. All calculations were performed using the Berry phase formalism implemented in VASP, which determines polarization as a geometric phase of the electronic wavefunctions, thus capturing the electronic contribution beyond simple point-charge models. The spontaneous polarization was then obtained as follows:

$$P_s = P_{\text{polar}} - P_{\text{centro}} \quad (1)$$

where P_{polar} and P_{centro} correspond to the Berry phase polarizations of the ferroelectric and centrosymmetric phases, respectively. Care was taken to identify the correct branch of polarization since the Berry phase is defined modulo a polarization quantum, ensuring that the final value corresponds to the physically meaningful polarization change along the distortion pathway. These calculations were carried out using the modern theory of polarization as implemented in VASP. The optical properties were calculated based on the frequency-dependent dielectric function, derived from the complex dielectric tensor $\varepsilon(\omega) = \varepsilon_1(\omega) + i\varepsilon_2(\omega)$. The imaginary part was computed from the interband transitions, and the real part was obtained using the Kramers–Kronig relations.

Results and discussion

Structural properties

Fig. 1 represents the systematic illustration of $HfMnO_3$. It has a trigonal structure with a polar space group of *R3C*. The unit cell contains ten atoms, corresponding to two formula units of $HfMnO_3$, where Hf and Mn occupy the A- and B-sites of the perovskite lattice, respectively, and the six oxygen atoms coordinate the Mn cations to form the MnO_6 octahedra. The atomic positions show clear deviations from centrosymmetric, with the oxygen atoms displaying off-symmetric locations that point to lattice distortion. Furthermore, it belongs to the non-centrosymmetric point group $3m$ (C_{3v}) with a three-fold

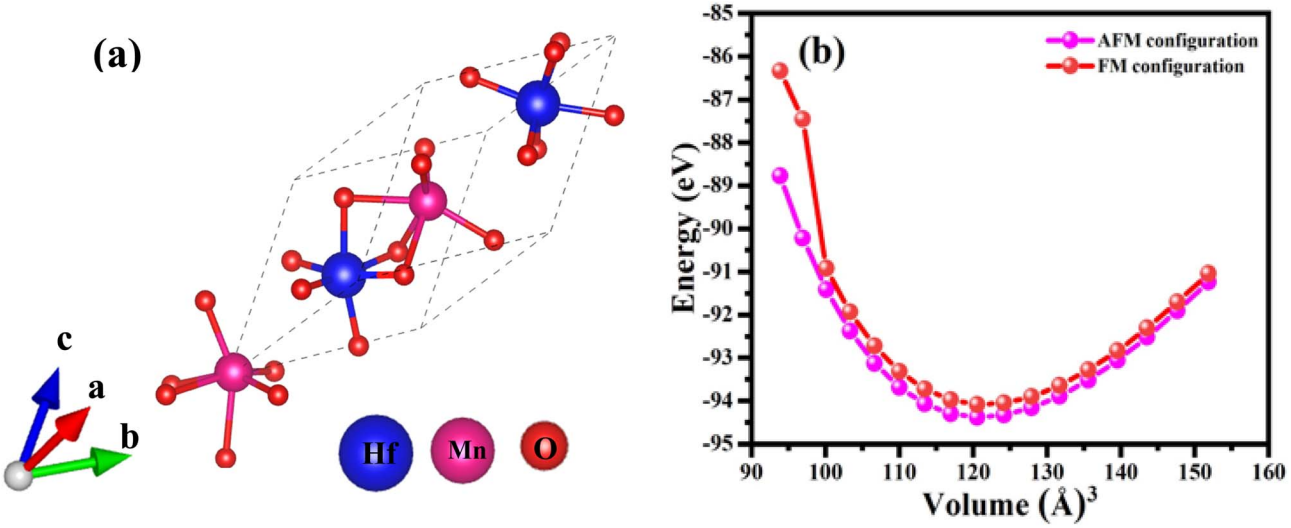

Fig. 1 (a) The structure of an altermagnet $HfMnO_3$ unit cell. (b) The obtained energy *vs.* volume curve for FM and stable AFM configurations.

rotational axis along [111]. In the antiferromagnetic state, the time-reversal symmetry (T) is broken, and inversion symmetry (P) is absent, meaning that combined PT symmetry does not exist. The lack of antiunitary symmetries such as PT ensures that Kramers degeneracy is lifted, allowing momentum-dependent spin splitting even without spin–orbit coupling. Unitary operations such as C_3 rotations and glide reflections interchange spin-sublattices, enforcing alternating spin polarization in k-space. These symmetry conditions clearly demonstrate that $HfMnO_3$ satisfies the requirements for altermagnetism. First, we determined the magnetic ground state and found that the antiferromagnetic (AFM) configuration is energetically favorable compared to the ferromagnetic (FM) configuration. The AFM state is more stable than the FM state by an energy difference of 270 meV per unit cell. The energy *versus* volume curve was calculated as shown in Fig. 1(b). The curves indicate that the AFM configuration is more stable than the FM configuration, and most probably, the FM and AFM states will be degenerate at more than 8% tensile strain. The obtained lattice constant was found to be 5.73 Å. After full optimization of the structure, we computed the formation energy of the $HfMnO_3$. The negative value of −2.1 eV per atom indicates that $HfMnO_3$ is thermodynamically stable. Furthermore, we computed the phonon dispersion curve to compute the dynamic stability of $HfMnO_3$. The obtained phonon dispersion band is plotted in Fig. 2, which reveals no imaginary frequency, indicating that $HfMnO_3$ is dynamically stable.

To assess the structural stability of $HfMnO_3$, we calculated the Goldschmidt tolerance factor (t), which provides insight into the geometric compatibility of ions within the perovskite lattice. Using the standard formula

$$\tau = \frac{r_A + r_X}{\sqrt{2}(r_B + r_X)} \quad (2)$$

where r_A, r_B and r_X are the ionic radii of Hf, Mn, and O, respectively, we obtained a tolerance factor of 0.88. This value falls within the typical range (0.7–0.92) associated with distorted perovskite structures, particularly those crystallizing in the $R3c$ (trigonal/rhombohedral) space group.[21,22] Therefore, the calculated tolerance factor supports the structural feasibility of $HfMnO_3$ adopting a distorted perovskite framework with tilted MnO_6 octahedra.

Electronic properties

Investigating the electronic properties of a material is essential for understanding its potential applications in spintronics, electronics, and energy conversion technologies. The electronic band structure provides direct insight into the nature of charge carriers, energy bandgap, spin polarization, and magnetic interactions. In particular, analyzing spin-resolved band structures enables the identification of spin-dependent phenomena such as half-metallicity, spin splitting, or altermagnetism,

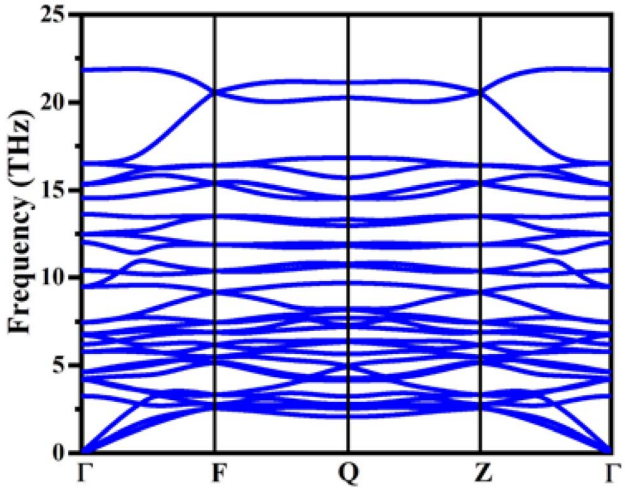

Fig. 2 The obtained phonon dispersion curve for the altermagnet $HfMnO_3$.

which are the critical characteristics for next-generation devices. Fig. 3(a) presents the spin-polarized electronic band structure of $HfMnO_3$, where the red and blue lines represent the spin-up and spin-down channels, respectively. A careful inspection reveals that the bands partially overlap in some directions, while a clear splitting exists between the spin-up and spin-down bands in other directions. This directional dependence of band splitting, without a net magnetization, is a key signature of altermagnetic behavior, a recently proposed magnetic phase that combines properties of both antiferromagnets and ferromagnets.[23] Fig. 3(b) shows a zoomed-in view of the band structure in the energy window from −0.55 eV to −0.88 eV, further clarifying the nature of spin splitting. This range highlights the splitting between spin bands more clearly. Notably, the bands near the Fermi level exhibited very small spin splitting, while at deeper energies, the splitting became more pronounced. For instance, at the third band, the energy difference between spin-up and spin-down states was found to be approximately 55 meV. This behavior suggests that the exchange interaction in $HfMnO_3$ is energy-dependent and more prominent in lower-lying states. To further elucidate the electronic properties, we computed both the total density of states (TDOS) and partial density of states (PDOS), as presented in Fig. 4(a) and (b).

The TDOS results are consistent with the electronic band structure, providing a comprehensive reflection of the system's electronic behavior, whereas the PDOS analysis revealed that the states near the Fermi level are dominated by Mn atom contributions. In the valence band, O exhibits a higher contribution compared to Hf, whereas in the conduction band, an opposite trend is observed. To more meaningfully study the electronic properties, we calculated the electronic charge density difference, which is presented in Fig. 5. The redistribution of charge is depicted using different colors, where blue indicates the charge depletion, while yellow represents the charge accumulation, *i.e.*, the area showing the blue color corresponds to regions experiencing a loss of charge, whereas those in the yellow color highlight zones with an enhanced charge presence. The figure shows that Mn and Hf are losing the charge while O is gaining the charge. This feature is attributed to the high electronegativity of O compared to Mn and Hf. Fig. 6 presents the spin density distribution of the $HfMnO_3$ system. Here, the yellow and blue isosurfaces correspond to regions dominated by spin-up and spin-down electrons, respectively, which specifically represent the spin-up and spin-down states of Mn atoms, revealing an alternating spin alignment within the lattice. The alternating colors localized around Mn atoms indicate an antiferromagnetic (AFM) ground state with compensated sublattices. As a result, neighboring Mn atoms adopt opposite spin orientations, leading to spin compensation between the Mn sublattices and a net-zero macroscopic magnetization. The compensated sublattices ensure that, despite the strong local moments, the net magnetization remains nearly zero. This distribution is consistent with the spin-polarized density of states, which shows unequal occupation of spin-up and spin-down bands. Altogether, the spin density distribution in $HfMnO_3$ demonstrates that Mn atoms carry dominant antiparallel moments. Such an antiferromagnetic ground state confirms the stability of spin ordering in $HfMnO_3$ and also highlights its potential relevance to altermagnetic phenomena, where compensated magnetic configurations can still produce spin-polarized band splitting due to lattice symmetry.

The observed spin-dependent band splitting without net magnetization positions $HfMnO_3$ as a promising altermagnetic material. This class of materials is gaining attention due to their potential to support spin-polarized currents without stray fields, making them ideal candidates for spintronic devices, magnetic sensors, and non-volatile memory technologies. Therefore, the combination of spin anisotropy and band splitting in $HfMnO_3$ may open pathways for novel device architectures that exploit the advantages of both antiferromagnetic robustness and spin-selective transport.

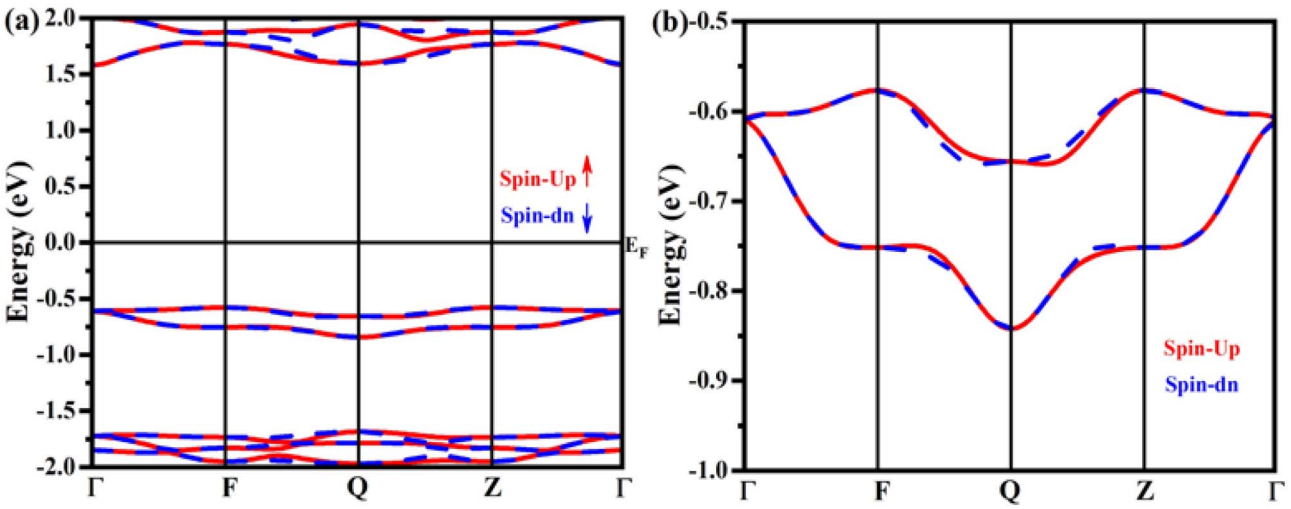

Fig. 3 The obtained spin-polarized band structure for the altermagnet $HfMnO_3$ in windows of (a) −2 eV to 2 eV and (b) −0.5 eV to −1.0 eV.

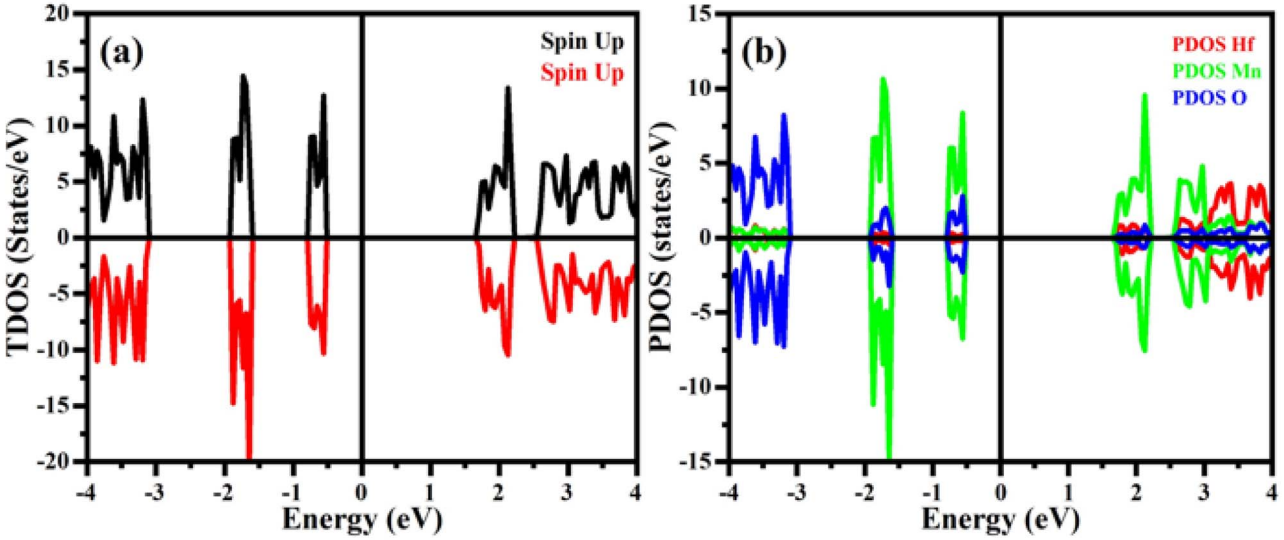

Fig. 4 The obtained density of states for the altermagnet $HfMnO_3$: (a) TDOS and (b) PDOS.

Ferroelectricity

Ferroelectricity refers to the existence of a spontaneous electric polarization that can be reversed by an external electric field. In perovskite oxides, ferroelectric behavior is often associated with the displacement of cations (such as A- or B-site ions) relative to the oxygen anions, breaking the inversion symmetry of the crystal structure. Studying the ferroelectric properties of materials like $HfMnO_3$ is crucial for their potential use in non-volatile memory, piezoelectric, and multiferroic applications. $HfMnO_3$ crystallizes in a trigonal structure with space group $R3c$ (No. 161), which is a polar space group allowing spontaneous polarization. The centrosymmetric reference phase has the space group $R\bar{3}c$ (No. 167), which possesses inversion symmetry and does not exhibit spontaneous polarization. To evaluate the ferroelectric nature of $HfMnO_3$, we calculated its spontaneous polarization using the Berry phase approach, a modern and widely accepted method implemented in VASP that accurately captures electronic contributions based on the geometric phase of the electronic wavefunctions.[24] The polarization of the polar (ferroelectric) and centrosymmetric (non-polar) reference structures is as follows:

$$P_s = P_{polar} - P_{centro} \quad (3)$$

The electronic contribution to polarization P can be expressed as a Berry phase integral over the Brillouin zone (BZ):[25]

$$P_s = \frac{e}{\Omega}\sum_i Z_i^* \vec{r_i} \quad (4)$$

Here, 'e' is the elementary charge, Ω is the volume of the unit cell, Z_i^* is the Born effective charge tensor of the ith atom, and $\vec{r}_i$ is the displacement vector of atom i along the polarization direction, in this case, the [111] axis. Our calculations predict a large spontaneous polarization of approximately 104 μC cm^{-2}

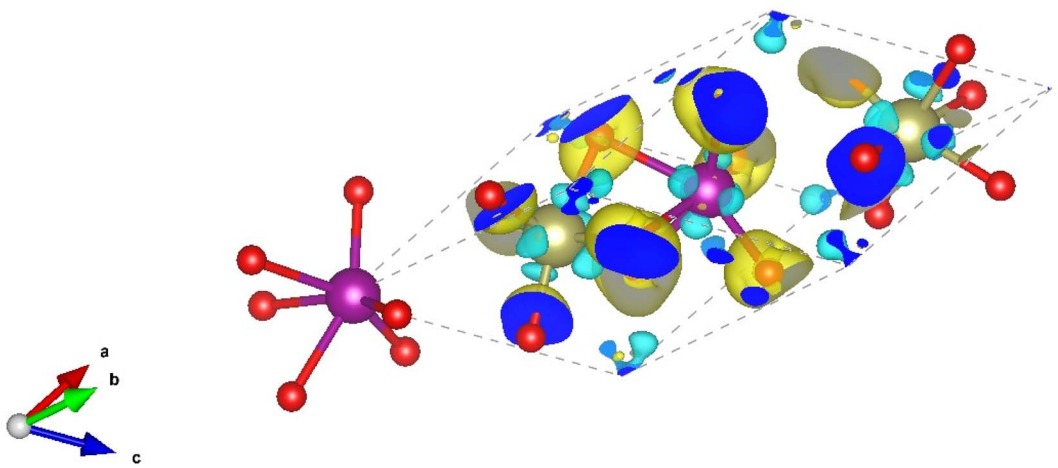

Fig. 5 The obtained charge density difference plots for the altermagnet $HfMnO_3$. Here, the isosurface value is considered to be 0.012.

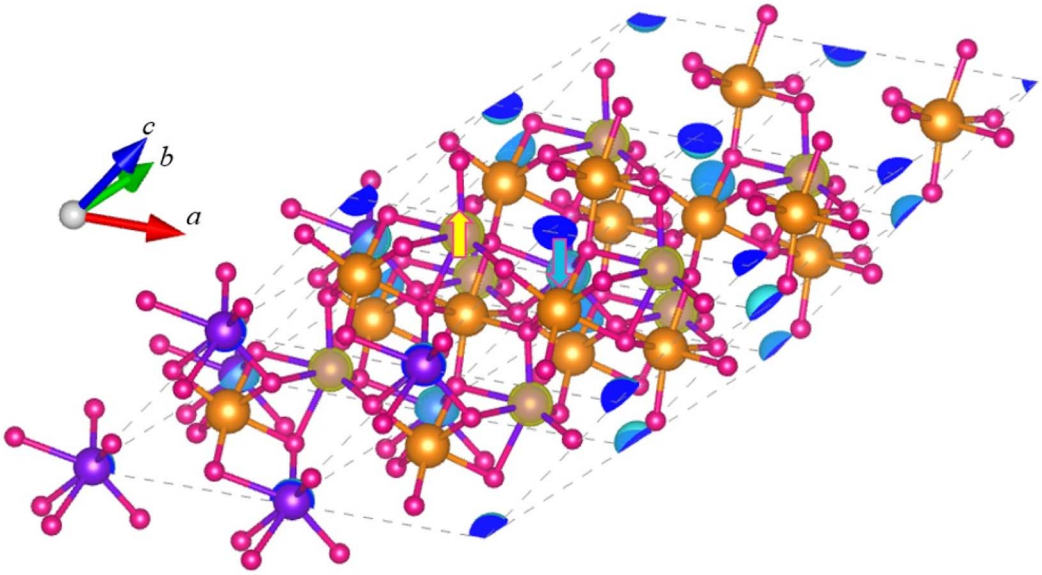

Fig. 6 The obtained spin density plots for the altermagnet $HfMnO_3$.

oriented along the [111] crystallographic direction, consistent with the symmetry axis of the *R*3*c* structure, as shown in Fig. 7. This polarization magnitude is comparable to well-studied ferroelectric perovskites such as $BiFeO_3$, which typically exhibit spontaneous polarizations in the range of 90–100 μC cm^{-2}.[26] The strong polarization in $HfMnO_3$ is primarily driven by significant off-centering displacements of Hf and Mn ions relative to the oxygen octahedra, which distort the lattice and break inversion symmetry. The [111] direction corresponds to the body-diagonal of the pseudo-cubic unit cell, a common polarization direction in rhombohedral perovskites due to their crystal symmetry.

Physically, the sizable polarization arises from the strong covalent interactions and hybridization between the transition metal d-orbitals and oxygen p-orbitals, which facilitate the ionic displacements and stabilize the ferroelectric phase. Compared to other reported materials with similar trigonal *R*3*c* symmetry, the polarization magnitude and direction in $HfMnO_3$ underscore its potential as a robust ferroelectric material with possible multiferroic coupling when combined with its magnetic ordering. Besides calculating the spontaneous polarization, we also investigated the dynamic stability of the structure at the polarization-switched state. The phonon dispersion curve, presented in Fig. 2, shows no imaginary frequencies throughout the Brillouin zone, confirming the dynamic stability of the switched ferroelectric phase. This ensures that the structure is mechanically stable and can sustain polarization switching without undergoing structural collapse or phase transformation. Furthermore, we computed the spin-polarized electronic band structure for the polarization-switched configuration shown in Fig. 8 and observed signatures of altermagnetic behavior, characterized by spin-split bands with compensated magnetization. The coexistence of altermagnetism and ferroelectricity in $HfMnO_3$ establishes it as

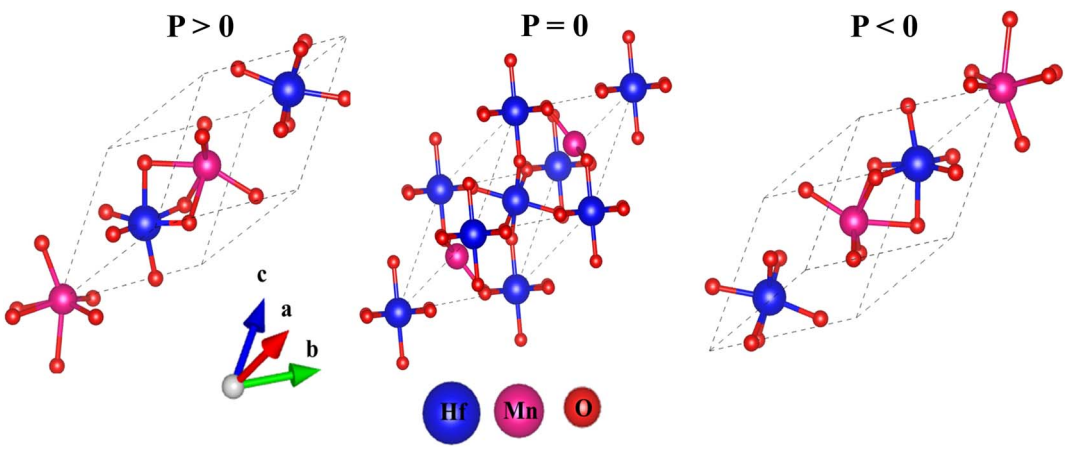

Fig. 7 The configuration of the altermagnet $HfMnO_3$ for switchable polarization.

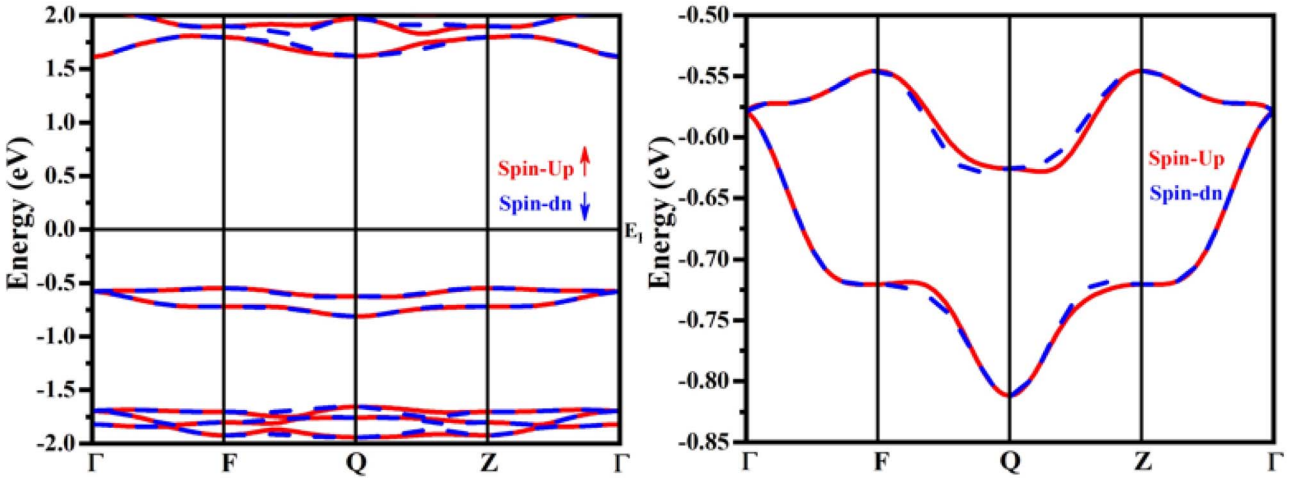

Fig. 8 The obtained spin-polarized band structure for switchable polarization ($P < 0$) of the altermagnet $HfMnO_3$ in windows of −2 eV to 2 eV and −0.5 eV to −0.85 eV.

a multiferroic material, which combines both magnetic and electric order parameters. This unique coupling opens promising opportunities for spintronic applications, where electric fields could control spin currents or magnetic states, enabling low-power, multifunctional devices. Thus, the robust multiferroic behavior in $HfMnO_3$ makes it a compelling candidate for future spintronic technologies.

Optical properties

Following a comprehensive analysis of the electronic and thermoelectric properties, we examined the optical characteristics of the $HfMnO_3$ altermagnet within the photon energy range of 0 to 12 eV. These optical properties include the real $\varepsilon_1(\omega)$ and imaginary $\varepsilon_2(\omega)$ parts of the dielectric function, absorption coefficient $\alpha(\omega)$, refractive index $n(\omega)$, reflectivity $R(\omega)$, and electron energy loss spectrum (EELS) $L(\omega)$. The frequency-dependent complex dielectric function $\varepsilon(\omega) = \varepsilon_1(\omega) + i\varepsilon_2(\omega)$ serves as the fundamental quantity describing the material's response to electromagnetic radiation and provides insight into its optical behavior. According to the Kramers–Kronig relations, the real part of the dielectric constant can be derived from the imaginary component through the principal value integral:[27]

$$\varepsilon_1(\omega) = 1 + \frac{2}{\pi} P \int_0^{\infty} \frac{\omega' \varepsilon_2(\omega)}{\omega'^2 - \omega^2} d\omega' \quad (5)$$

The imaginary part $\varepsilon_2(\omega)$, which reflects the absorption due to electronic transitions from occupied to unoccupied states across the Brillouin zone, is given by the following:

$$\varepsilon_2(\omega) = \frac{8}{2\pi\omega^2} \sum_{nn'} \int |p_{nn'}(k)|^2 \frac{dS_k}{\nabla \omega_{nn'}(ks)} \quad (6)$$

Other optical constants, including the refractive index, $n(\omega)$, reflectivity $R(\omega)$, electron energy loss spectrum (EELS) $L(\omega)$, and absorption coefficient $\alpha(\omega)$ can be computed by using the following relation:[28]

$$n(\omega) = \left[\frac{\sqrt{\varepsilon_1^2(\omega) + \varepsilon_2^2(\omega)}}{2} + \frac{\varepsilon_1(\omega)}{2} \right]^{1/2} \quad (7)$$

$$\alpha(\omega) = \left[\sqrt{\varepsilon_1^2(\omega) + \varepsilon_2^2(\omega)} - \varepsilon_1(\omega) \right]^{1/2} \quad (8)$$

$$R(\omega) = \frac{(1-n)^2 + k^2}{(1+n)^2 + k^2} \quad (9)$$

$$\mathrm{ELF} = \frac{\varepsilon_2}{\varepsilon_1^2 + \varepsilon_2^2} \quad (10)$$

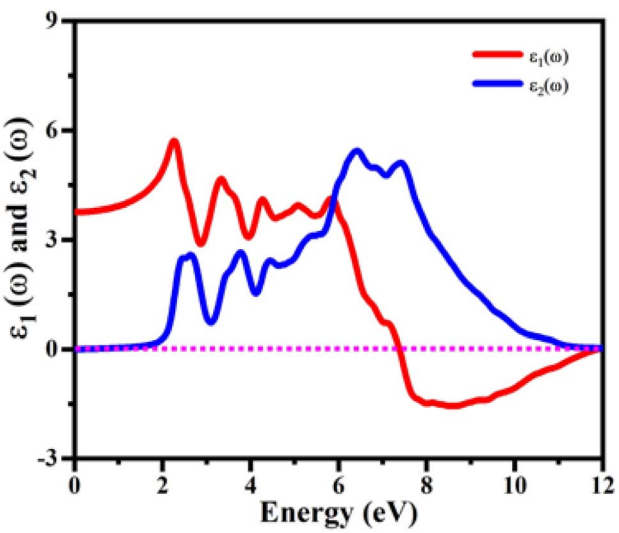

Fig. 9 The obtained dielectric function for the real and imaginary parts of the altermagnet $HfMnO_3$.

Fig. 9 illustrates the real part of the dielectric function, $\varepsilon_1(\omega)$, which reflects the material's capacity to polarize in response to incoming electromagnetic waves. This polarization directly influences how light propagates and disperses through the material. According to our results, the static dielectric constant $\varepsilon_1(0)$ was calculated to be 3.91. From zero photon energy, $\varepsilon_1(\omega)$ gradually increases, reaching a maximum value of approximately 5.89 at around 2.2 eV. Following this peak, the function exhibits several smaller peaks before sharply declining near 6 eV. Beyond 7 eV, the real part of the dielectric function turns negative, indicating a transition in optical behavior. Notably, at photon energies exceeding approximately 7.5 eV, $\varepsilon_1(\omega)$ becomes negative, signaling a metallic response characterized by the excitation of plasmons, which are collective oscillations of free electrons.[28] This negative dielectric permittivity in the high-energy regime implies that $HfMnO_3$ strongly reflects incident light, demonstrating high reflectivity and supporting plasmonic behavior. These optical responses are governed by the electronic band structure and interband transitions that dominate the absorption and dispersion of light in the material. The presence of plasmonic features suggests potential applications in optoelectronic devices and plasmonic technologies, where strong light–matter interaction is desired.

Fig. 9 displays the imaginary component of the dielectric function $\varepsilon_2(\omega)$, which quantifies the material's ability to absorb incident electromagnetic radiation. This quantity is directly linked to the energy absorbed when photons promote electrons from occupied states in the valence band to unoccupied states in the conduction band, representing interband electronic transitions.[29] In the case of $HfMnO_3$, the value of $\varepsilon_2(\omega)$ remains close to zero, up to about 1.7 eV, indicating very low absorption at lower photon energies. Above this energy, a broad absorption feature appears, extending to nearly 10 eV, with the highest peak observed near 6.2 eV where $\varepsilon_2(\omega)$ attained its maximum around 5.4. These absorption characteristics arise from electronic excitations at key symmetry points within the Brillouin zone, as indicated by the electronic band structure. The absorption edge at 1.7 eV marks the threshold energy required to excite electrons across the band gap. The wide absorption in the ultraviolet range is due to numerous allowed transitions between deeper valence bands and higher conduction bands. This strong optical absorption behavior reflects the intimate connection between the electronic structure and the optical response and suggests that $HfMnO_3$ could be a promising candidate for ultraviolet photodetection and other optoelectronic applications where strong light–matter interaction is essential.[30]

Further, our calculations revealed that $HfMnO_3$ possesses a direct band gap, which implies that the lowest energy optical transitions occur without the need for phonon assistance, resulting in a sharp absorption edge. The features observed in the imaginary part of the dielectric function and the absorption spectra can be directly attributed to interband electronic transitions. Since the material is a direct-gap semiconductor, the optical absorption edge is determined primarily by these direct transitions, rather than being suppressed by indirect gap constraints. Besides, the presence of a direct band gap suggests that strong excitonic effects are unlikely to dominate in this material, as the onset of absorption is well aligned with the fundamental gap. Therefore, the detailed optical response, such as the prominent peaks in dielectric functions, originates from band-to-band transitions consistent with the electronic band structure. These clarifications have been incorporated into the revised manuscript to provide a more complete physical understanding of the optical behavior.

The refractive index (ω) characterizes how light behaves as it passes through a material, providing insight into the degree of bending or refraction experienced by the incident light.[31] Fig. 10(a) presents the variation of $n(\omega)$ for $HfMnO_3$. The static refractive index (0) was calculated to be approximately 1.97. As photon energy increases, the refractive index gradually rises, reaching a peak value of around 2.4 at about 2 eV, which lies within the visible spectrum. This increase suggests strong interactions of light with the electronic states of the material at lower energies. Beyond this point, the refractive index remains relatively steady before exhibiting a sharp decline after 5.8 eV, indicating a significant reduction in the material's ability to refract high-energy photons. This downward trend signifies that the optical density of the material drops at higher energies, particularly in the ultraviolet region. The observed behavior of (ω) closely follows the real part of the dielectric function $\varepsilon_1(\omega)$, which is expected since both quantities are related by the following relation: $n(0) = \sqrt{\varepsilon_1(0)}$. The consistency between these two optical parameters reaffirms the reliability of the calculated data. Given the notable refractive index in the visible to near-UV range, $HfMnO_3$ may be considered a viable candidate for use as an intermediate optical layer in devices designed to manage or manipulate UV light, such as UV filters, coatings, or waveguides.

The optical absorption spectrum of $HfMnO_3$ is depicted in Fig. 10(b). The absorption coefficient (ω), which is directly derived from the imaginary part of the dielectric function $\varepsilon_2(\omega)$, provides insight into the material's ability to absorb incident electromagnetic radiation. It describes the exponential attenuation of light intensity as it propagates through the material and is essential for assessing the optoelectronic applicability of the compound.[32] In the case of $HfMnO_3$, the absorption edge begins around 2.0 eV, indicating that the material starts to absorb photons in the visible region of the electromagnetic spectrum. As the photon energy increases, the absorption gradually intensifies, showing a broad and strong absorption band in the 6–12 eV range, which lies in the ultraviolet (UV) region. This broad UV absorption indicates a high photon capture capability, making $HfMnO_3$ a suitable candidate for UV photodetectors and protective coatings against harmful UV radiation. A notable absorption peak is observed at approximately 9.0 eV, with a maximum absorption coefficient value reaching 1.5×10^{-6} cm^{-1}. Such a high absorption intensity further underscores the compound's excellent potential for UV optoelectronic applications. Moreover, the absorption coefficient remains relatively low in the lower-energy visible region (below 2 eV), suggesting that $HfMnO_3$ exhibits optical transparency in this regime. This transparent behavior in the visible region opens up

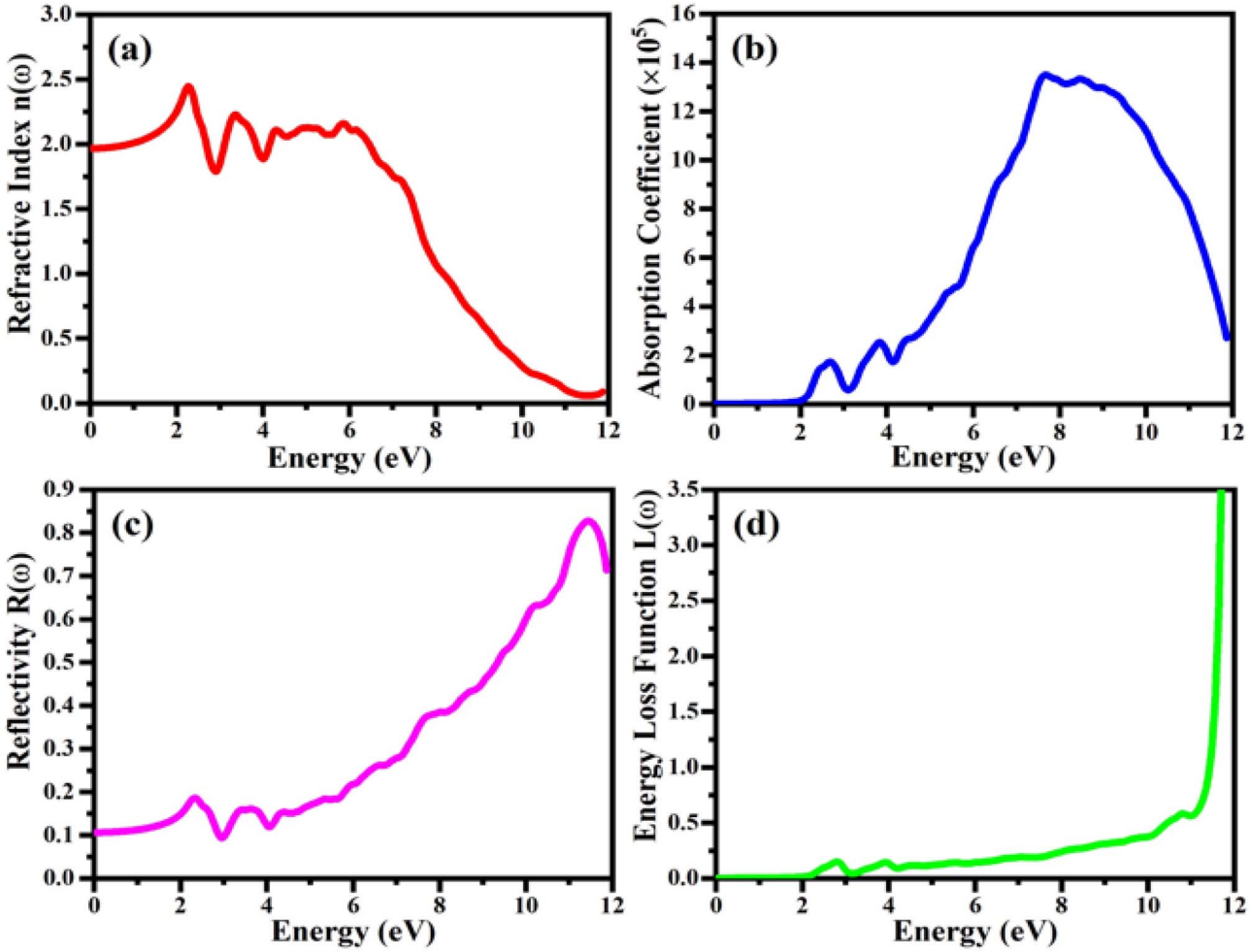

Fig. 10 The obtained optical parameters for the altermagnet $HfMnO_3$: (a) refractive index, (b) absorption coefficient, (c) reflectivity, and (d) energy loss function.

the possibility of utilizing $HfMnO_3$ as a transparent electrode or buffer layer in solar cells or other multilayer optoelectronic devices. The ability to allow visible light transmission while absorbing higher-energy UV photons could enhance the overall efficiency and longevity of devices by maximizing light harvesting and minimizing UV-induced degradation.

The reflectivity behavior of $HfMnO_3$ as a function of photon energy is illustrated in Fig. 10(c). At zero photon energy, the initial reflectivity (0) was calculated to be approximately 15%, indicating that a relatively small fraction of incident light is reflected at very low energies. This low initial reflectance implies that most of the low-energy photons can enter the material, contributing to its absorption behavior. As the photon energy increases, the reflectivity gradually rises. In the visible spectrum, the reflectivity remains below 40%, suggesting that the material does not significantly reflect visible light. This observation aligns well with the absorption characteristics, confirming that visible light is primarily absorbed or transmitted through the compound rather than reflected. Beyond the visible region, particularly in the ultraviolet range, the reflectivity exhibits a sharp increase, reaching a maximum value of approximately 80% at 12 eV. This substantial rise in the UV domain indicates that $HfMnO_3$ begins to behave more like a metallic reflector at high photon energies. The increase in reflectivity corresponds to the regions where the real part of the dielectric function becomes negative, a typical indicator of plasma resonance or metallic optical response. The strong reflectivity in the UV range implies potential applications for $HfMnO_3$ in devices requiring UV mirrors or protective coatings, while its moderate to low reflectivity in the visible region supports its transparency and absorption efficiency for solar and optoelectronic technologies.

The electron energy loss spectrum (EELS), represented by the energy loss function, $L(\omega)$, provides insight into the energy dissipated by fast-moving electrons as they traverse a material under the influence of incident electromagnetic radiation.[33] The calculated (ω) for $HfMnO_3$ is shown in Fig. 10(d). In this context, the energy loss is primarily associated with plasmonic excitations, which result from the collective oscillations of conduction electrons stimulated by external electromagnetic fields. Peaks in $HfMnO_3$ are indicative of plasma resonance frequencies, signifying significant electron oscillation and energy loss

within the system. For $HfMnO_3$, the energy loss function remains very low (below 1) in the low photon energy range up to approximately 8 eV, indicating minimal energy dissipation in this region. This suggests that the compound does not exhibit notable plasmonic activity at lower energies, which complements earlier findings that most visible light is absorbed or transmitted rather than contributing to electronic excitation losses. However, beyond 8 eV, a gradual rise in the energy loss function is observed, reaching a prominent peak of around 5 at 12 eV. This peak indicates the presence of a plasmon resonance, marking the energy at which collective electron oscillations lead to significant energy dissipation. The sharp increase in (ω) at higher photon energies confirms the onset of strong interband transitions and energy loss phenomena in the ultraviolet regime. Such behavior is characteristic of materials with the potential for plasmonic and high-frequency optoelectronic applications, where control of electron energy dissipation is essential.

Conclusion

In this work, we have comprehensively investigated the structural, electronic, ferroelectric, and optical properties of trigonal perovskite $HfMnO_3$ using first-principles density functional theory (DFT) calculations. Our results confirm that $HfMnO_3$ crystallizes in a distorted *R3c* polar structure with a negative formation energy and phonon spectrum free of imaginary frequencies, indicating thermodynamic and dynamic stability. The spin-polarized band structure reveals direction-dependent spin splitting without net magnetization, a clear signature of altermagnetic ordering. This exotic magnetic behavior combines the advantages of ferromagnets and antiferromagnets, offering the potential for spintronic devices with low power consumption and no stray fields. Furthermore, $HfMnO_3$ exhibits a large spontaneous polarization of approximately 104 $\mu C\ cm^{-2}$ along the [111] direction, as calculated *via* the Berry phase method. This polarization arises from the asymmetric displacement of cations and hybridization between Mn d-orbitals and O p-orbitals, confirming robust ferroelectric behavior. The coexistence of altermagnetism and ferroelectricity in a single phase establishes $HfMnO_3$ as a promising multiferroic material, suitable for non-volatile memory, magnetic sensors, and electric-field-controlled spintronic applications. Optical analyses reveal strong ultraviolet absorption, moderate dielectric constants, and a plasmonic resonance region above 7.5 eV. These features suggest that $HfMnO_3$ could also be utilized in UV photodetectors, transparent coatings, and plasmonic devices. In summary, $HfMnO_3$ emerges as a multifunctional material with coexisting altermagnetic, ferroelectric, and optical properties, making it a strong candidate for future applications in multiferroic and spintronic technologies.

Conflicts of interest

The authors declare no conflict of interest.

Data availability

The data will be made available on reasonable request.

Acknowledgements

The authors extend their appreciation to the Deanship of Research and Graduate Studies at King Khalid University, Kingdom of Saudi Arabia for funding this work through the Large Research Group Project under the grant number RGP. 2/146/46. The authors extend their appreciation to the Deanship of Scientific Research at Northern Border University, Arar, KSA for funding this research work through the project number NBU-FFR-2025-2483-19.

References

1 L. Šmejkal, J. Sinova and T. Jungwirth, Emerging research landscape of altermagnetism, *Phys. Rev. X*, 2022, **12**(4), 040501.
2 R. González-Hernández, H. Serrano and B. Uribe, Spin Chern number in altermagnets, *Phys. Rev. B*, 2025, **111**(8), 085127.
3 C. C. Wei, E. Lawrence, A. Tran and H. Ji, Crystal chemistry and design principles of altermagnets, *ACS Org. Inorg. Au*, 2024, **4**(6), 604–619.
4 T. Osumi, S. Souma, T. Aoyama, K. Yamauchi, A. Honma, K. Nakayama, T. Takahashi, K. Ohgushi and T. Sato, Observation of a giant band splitting in altermagnetic MnTe, *Phys. Rev. B*, 2024, **109**(11), 115102.
5 S. Chen, D. J. Lin, B. C. Lim and P. Ho, Mn-based noncollinear antiferromagnets and altermagnets, *J. Phys. D: Appl. Phys.*, 2024, **57**(44), 443001.
6 O. Fedchenko, J. Minár, A. Akashdeep, S. W. D'Souza, D. Vasilyev, O. Tkach, L. Odenbreit, Q. Nguyen, D. Kutnyakhov, N. Wind and L. Wenthaus, Observation of time-reversal symmetry breaking in the band structure of altermagnetic RuO_2, *Adv. Sci.*, 2024, **10**(5), eadj4883.
7 X. Peng, Y. Wang, S. Zhang, Y. Zhou, Y. Sun, Y. Su, C. Wu, T. Zhou, L. Liu, H. Wang and J. Yang, Scaling behavior of magnetoresistance and Hall resistivity in the altermagnet CrSb, *Phys. Rev. B*, 2025, **111**(14), 144402.
8 Z. Li, Z. Zhang, Y. Chen, S. Hu, Y. Ji, Y. Yan, J. Du, Y. Li, L. He, X. Wang and J. Wu, Fully Field-Free Spin–Orbit Torque Switching Induced by Spin Splitting Effect in Altermagnetic RuO_2, *Adv. Mater.*, 2025, **37**(12), 2416712.
9 J. Krempaský, L. Šmejkal, S. W. D'souza, M. Hajlaoui, G. Springholz, K. Uhlířová, F. Alarab, P. C. Constantinou, V. Strocov, D. Usanov and W. R. Pudelko, Altermagnetic lifting of Kramers spin degeneracy, *Nature*, 2024, **626**(7999), 517–522.
10 C. Song, H. Bai, Z. Zhou, L. Han, H. Reichlova, J. H. Dil, J. Liu, X. Chen and F. Pan, Altermagnets as a new class of functional materials, *Nat. Rev. Mater.*, 2025, **14**, 1–13.
11 G. H. Al-Hazmi, A. Zaman, N. Akhter, S. H. Alrefaee, P. Ahmad, T. Orlova, A. Nurmuhammedov, V. Tirth, A. Algahtani and N. M. Hadia, Structural, Electronic and

Optical Properties of Altermagnet Bulk $MnBr_2$, *Int. J. Quantum Chem.*, 2025, **125**(7), e70031.

12 Q. Zhang, T. Cagin and W. A. Goddard III, The ferroelectric and cubic phases in $BaTiO_3$ ferroelectrics are also antiferroelectric, *Proc. Natl. Acad. Sci. U. S. A.*, 2006, **103**(40), 14695–14700.

13 F. Kubel and H. Schmid, Structure of a ferroelectric and ferroelastic monodomain crystal of the perovskite $BiFeO_3$, *Struct. Sci.*, 1990, **46**(6), 698–702.

14 R. E. Cohen and H. Krakauer, Electronic structure studies of the differences in ferroelectric behavior of $BaTiO_3$ and $PbTiO_3$, *Ferroelectrics*, 1992, **136**(1), 65–83.

15 W. Ji, K. Yao and Y. C. Liang, Bulk photovoltaic effect at visible wavelength in epitaxial ferroelectric $BiFeO_3$ thin films, *Adv. Mater.*, 2010, **22**(15), 1763.

16 M. Gu, Y. Liu, H. Zhu, K. Yananose, X. Chen, Y. Hu, A. Stroppa and Q. Liu, Ferroelectric switchable altermagnetism, *Phys. Rev. Lett.*, 2025, **134**(10), 106802.

17 M. Gu, Y. Liu, H. Zhu, K. Yananose, X. Chen, Y. Hu, A. Stroppa and Q. Liu, Ferroelectric switchable altermagnetism, *Phys. Rev. Lett.*, 2025, **134**(10), 106802.

18 W. Sun, C. Yang, W. Wang, Y. Liu, X. Wang, S. Huang and Z. Cheng, Proposing Altermagnetic-Ferroelectric Type-III Multiferroics with Robust Magnetoelectric Coupling, *Adv. Mater.*, 2025, **10**, 2502575.

19 Z. Zhu, X. Duan, J. Zhang, B. Hao, I. Žutić and T. Zhou, Two-Dimensional Ferroelectric Altermagnets: From Model to Material Realization, *Nano Lett.*, 2025, **25**(23), 9456–9462.

20 W. Sun, W. Wang, C. Yang, R. Hu, S. Yan, S. Huang and Z. Cheng, Altermagnetism induced by sliding ferroelectricity *via* lattice symmetry-mediated magnetoelectric coupling, *Nano Lett.*, 2024, **24**(36), 11179–11186.

21 C. J. Bartel, C. Sutton, B. R. Goldsmith, R. Ouyang, C. B. Musgrave, L. M. Ghiringhelli and M. Scheffler, New tolerance factor to predict the stability of perovskite oxides and halides, *Adv. Sci.*, 2019, **5**(2), eaav0693.

22 Y. Luo, H. Tian, X. Li, L. Chen, Y. Yang and D. Wu, Diversity of structural phases in A Ge X 3 halides, *Phys. Rev. B*, 2022, **106**(2), 024112.

23 C. Song, H. Bai, Z. Zhou, L. Han, H. Reichlova, J. H. Dil, J. Liu, X. Chen and F. Pan, Altermagnets as a new class of functional materials, *Nat. Rev. Mater.*, 2025, **14**, 1–13.

24 C. Li, S. Yuan, Y. Li, Z. Wu, Y. Jin, K. P. Loh and K. Leng, Phonon Driven Ferroelectricity and Raman Active Modes in Hybrid Organic-Inorganic Perovskites, *Adv. Mater.*, 2025, 2419685.

25 H. Qiu, M. Yang and H. Huang, DFT-Machine Learning Joint Exploration of Transition Metal-Doped Ferroelectric $BaTiO_3$ for Electrocatalytic Hydrogen Evolution, *ACS Appl. Mater. Interfaces*, 2025, **17**(24), 35396–35408.

26 S. Saurabh, B. Kumar, N. Chauhan, V. Dwivedi, H. Tamang, S. Dahiya, A. Singh, A. Kumar, S. K. Srivastava and A. K. Singh, Impact of sintering temperature on the structural, ferroelectric, dielectric, and electrochemical properties of $BiFeO_3$ nanoparticles, *Inorg. Chem. Commun.*, 2025, **176**, 114262.

27 N. Akhter, S. H. Alrefaee, A. Nurmuhammedov, M. Soliyeva, P. Ahmad, V. Tirth, A. Algahtani, Q. Mohsen, O. Alsaqer, N. M. Hadia and A. Zaman, Strain-dependent structural, electronic, mechanical, optical and thermoelectric properties of Sr_3NBr_3 perovskites for solar cell applications, *Phys. Chem. Chem. Phys.*, 2025, **27**(6), 3160–3170.

28 M. U. Ghani, M. Junaid, K. M. Batoo, M. F. Ijaz and B. Zazoum, An extensive study of structural, electronic, optical, mechanical, and thermodynamic properties of inorganic oxide perovskite materials $ScXO_3$ (X = Ga, In) for optoelectronic applications: a DFT study, *Inorg. Chem. Commun.*, 2025, **172**, 113459.

29 A. Zaman, S. H. Alrefaee, M. Elhadi, P. Ahmad, M. Soliyeva, N. Akhter, N. Elboughdiri, V. Tirth, A. Algahtani, A. M. Alsuhaibani and M. S. Refat, First principles insight into Cs_2YZnX_6 (X = Br, I) double perovskite materials for optoelectronic and thermoelectric device applications, *Phys. Chem. Chem. Phys.*, 2025, **27**(24), 13043–13058.

30 S. Noola, G. Shankar, F. De Rossi, E. Calabrò, M. Bonomo, C. Barolo and F. Brunetti, Cuprous thiocyanate as an inorganic hole transport material for carbon-based flexible perovskite solar cells, *Sustainable Energy Fuels*, 2025, **9**(7), 1786–1796.

31 G. Murtaza, A. Ayyaz, M. B. Shakir, M. Touqir, K. Iqbal, A. Usman, S. Mumtaz and I. M. Moussa, Structural stability, optoelectronic, thermoelectric, and elastic characteristics of X_2ScBiO_6 (X = Mg, Ca, and Ba) double perovskites for energy harvesting: first-principles analysis, *Mater. Sci. Semicond. Process.*, 2025, **185**, 108911.

32 H. Ullah, Z. Nazir, A. Ahmad, M. Mushtaq, K. M. Alotaibi, K. Safeen and A. Safeen, Optoelectronics and thermoelectric response of halide-based perovskites $CsXY_3$ (X = Sn and Pb; Y = Cl, Br and I) semiconductors for solar cells and renewable energy, *J. Korean Phys. Soc.*, 2025, **86**(9), 892–908.

33 A. Zaman, S. H. Alrefaee, M. Elhadi, P. Ahmad, M. Soliyeva, N. Akhter, N. Elboughdiri, V. Tirth, A. Algahtani, A. M. Alsuhaibani and M. S. Refat, First principles insight into Cs2YZnX6 (X = Br, I) double perovskite materials for optoelectronic and thermoelectric device applications, *Phys. Chem. Chem. Phys.*, 2025, **27**(24), 13043–13058.